Vietnam Journal of Science and Technology ***64***(1) (2026) 87–99
DOI: https://doi.org/10.15625/2525-2518/19643

Investigating the photocatalytic activity in bactericidal effect of iron(III) oxide bi-phase composite against *Staphylococcus aureus*

Tan Muon Dinh[1,2,3], Nguyen Thanh Loan[3,4], Hoang Hung Nguyen[3,4], Tran Viet Cuong[3,4], Vinh Quang Dang[1,2], Huynh Tran My Hoa[3,4,*]

[1]*Faculty of Materials Science and Technology, University of Science, Ho Chi Minh City, Viet Nam*
[2]*Vietnam National University, Vo Truong Toan Street, Linh Trung Ward, Ho Chi Minh City, Viet Nam*
[3]*VKTECH Research Center, NTT Hi-Tech Institute, Nguyen Tat Thanh University, Vo Chi Cong Street, Long Thanh My Ward, Ho Chi Minh City, Viet Nam*
[4]*Center for Hi-Tech Development, Nguyen Tat Thanh University, Saigon Hi-Tech Park, Vo Chi Cong Street, Long Thanh My Ward, Ho Chi Minh City, Viet Nam*

[*]Email: *htmhoa@ntt.edu.vn*

Received: 12 December 2023; Accepted for publication: 31 July 2024

Abstract. This work describes the phase transition process used to create a bi-phase composite (called "α/γ-Fe_2O_3") from two iron precursors ($FeSO_4$ and $FeCl_3$). It was discovered that controlling the temperature between 200 and 800 °C was effective in both producing γ-Fe_2O_3 nanoparticles and initiating the phase transition of γ-Fe_2O_3 into α-Fe_2O_3 nanoparticles. The formation of a bi-phase mixture (α/γ-Fe_2O_3) occurred at 500 °C when the phase transition process was taking place. Consequently, the bactericidal efficiency of this bi-phase α/γ-Fe_2O_3 composite was more excellent than that of the single-phase α-Fe_2O_3 or γ-Fe_2O_3 material (from 1.1 to 1.6 times, respectively). Here, the bi-phase contacts probably formed between the α- and γ-phase nanoparticles of Fe_2O_3 played an important role in reducing the electron-hole recombination, and thus, increasing the photocatalytic and bactericidal efficiency of the developed composite material. Overall, our findings highlight the potential of this bi-phase material for practical photocatalytic applications.

Keywords: iron oxide, bi-phase, photocatalytic, bactericidal activity, *Staphylococcus aureus*.

Classification numbers: 2.4.2.

1. INTRODUCTION

Staphylococcus aureus (*S. aureus*) is an anaerobic bacterium frequently present on the skin, respiratory system, and nasal passages [1]. *S. aureus* enters the body by binding to surfaces like the skin and nasal cavity, aided by secretory agents [2]. This process can lead to various infectious conditions, encompassing minor skin and soft tissue infections, infective endocarditis, osteomyelitis, bacteremia, and life-threatening pneumonia [3]. It is estimated that *S. aureus* bacteremia has an incidence ranging from 20 to 50 cases per 100,000 cases of skin infections

yearly, and 10 % to 30 % of these patients die from the infection, placing a significant burden on the public health system [4]. Therefore, pre-emptive eradication of *S. aureus* prior to host attachment assumes critical significance. Currently, several methods, such as high-intensity UV-C light [5-7], chemical disinfection of surfaces [8], and antibiotics [9], are employed for *S. aureus* bactericidal. Besides, there has been a growing interest in photocatalytic activity (assisting in using antibiotics) as an alternative avenue of exploration. Scientific researchers have demonstrated the effective antibacterial properties of conventional semiconductor oxides (e.g., TiO_2 and ZnO) through photocatalysis [10, 11]. However, their wide bandgaps limit their photocatalytic functions under visible light irradiation, despite visible light constituting 43 % of the solar spectrum [12]. As a result, semiconductor oxides having small bandgaps and being active under visible light have drawn much attention, such as CuO, Bi_2O_3, WO_3, Fe_2O_3, and CdS [13]. Among them, the Fe_2O_3 is of great interest due to its abundance, inexpensiveness, ease of synthesis, non-toxicity, and chemical stability [14]. Especially, the Fe_2O_3 can appear in four different phases: α-Fe_2O_3, β-Fe_2O_3, γ-Fe_2O_3, and ε-Fe_2O_3 [15]. Notably, the bandgap values of α-Fe_2O_3 and γ-Fe_2O_3 range from 2.0 to 2.4 eV, which are appropriate for maximizing the photocatalytic activity under visible light [16, 17].

Recently, Pallela *et al.* [18] and Rana *et al.* [19] have reported the antibacterial efficacies of α-Fe_2O_3 and γ-Fe_2O_3 against *S. aureus*, respectively. Their proposed mechanism for bacterial eradication involves the generation of reactive oxygen species (ROS), including hydroxyl radicals (·OH), hydrogen peroxide (H_2O_2), and superoxide ($\cdot O^{2-}$), when α-Fe_2O_3 and γ-Fe_2O_3 were excited under visible light. That generated free radicals, which can disrupt polysaccharide activity, inactivate enzymes, induce DNA fragmentation, and initiate lipid peroxidation processes, ultimately leading to bacterial death. The fast recombination of electrons and holes in the single-phase γ-Fe_2O_3 or α-Fe_2O_3 material is an issue for its photocatalytic activity. It was followed by a shortage of electron and hole migrations to the material's surface, resulting in a continuous decline in the ROS production and thereby decreasing the antibacterial efficacy [20]. To address this problem, researchers have proposed employing heterojunctions to eliminate electron and hole recombination and enhance photocatalytic efficacy [21, 22]. However, to form either junctions or contacts based on the γ-Fe_2O_3 or α-Fe_2O_3, it is often necessary to utilize different types of materials, which can potentially result in alterations to the properties of Fe_2O_3. Interestingly, the Fe_2O_3 possesses a phase transition from γ-Fe_2O_3 to α-Fe_2O_3 at high temperatures. By controlling the phase transition temperature, a bi-phase contact between the α- and γ- phases can be formed, and it is promising for reducing electron-hole recombination and enhancing photocatalytic efficiency [23, 24].

In this work, we developed the bi-phase composite based on α- and γ-Fe_2O_3, and we investigated not only its photocatalytic activity but also its antibacterial activity against *S. aureus*. Through characterizations, the bactericidal ability of single-phase α-Fe_2O_3 or γ-Fe_2O_3 samples was found to be 51.54 % or 76.67 %, respectively. Meanwhile, the bi-phase α/γ-Fe_2O_3 samples exhibited outstanding bactericidal efficiency of up to 84.62 % under the same testing conditions of material utilization. This finding confirms the potential and effectiveness of replacing conventional single-phase materials with bi-phase materials in order to prevent electron-hole recombination for photocatalysis applications.

2. EXPERIMENTAL METHOD

2.1. Fabrication of α/γ-Fe_2O_3 bi-phase mixture

The synthesis procedure is illustrated in Figure 1. Briefly, 40 mL of a 0.25 M $FeSO_4$ solution was prepared by adding $FeSO_4.7H_2O$ (Sigma-Aldrich, purity ≥ 98 %) to distilled water and followed by heating at 70 °C. The solution was then filled with 40 mL of 0.5 M $FeCl_3.H_2O$ (Sigma-Aldrich, purity 97 %) so that the molar ratio of $2Fe^{3+}$:Fe^{2+} was reached. After stirring for 15 min, 30 mL of 5 M NaOH was gradually added to the solution until black precipitates were observed. The solution was further stirred for 60 min, then centrifuged, and washed several times with distilled water and ethanol to obtain Fe_3O_4 powder. In the final step, the prepared samples were calcined at various temperatures, including 200, 500, and 800 °C for 3 hours in the atmosphere, to produce the structures of γ-Fe_2O_3, α/γ-Fe_2O_3, and α-Fe_2O_3, respectively.

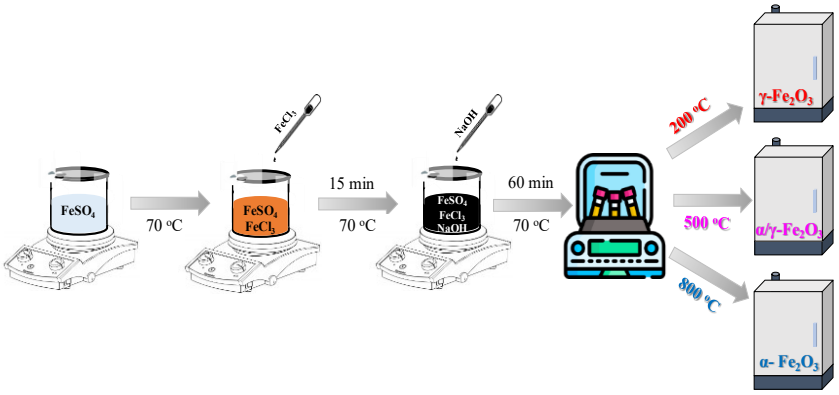

Figure 1. Synthesis process of γ-Fe_2O_3, α/γ-Fe_2O_3, and α-Fe_2O_3.

2.2. Characterization

The crystalline structure of synthesized samples was analyzed using X-ray diffraction (XRD-D8 Advanced) with monochromatic Cu-Kα radiation (λ = 1.54 Å) and Raman spectroscopy (Horiba XploRA Plus) with a 532 nm laser excitation source. The material's morphology and optical properties were investigated using Scanning Electron Microscopy (SEM-JEOL JSM-7600F) and Ultraviolet-Visible spectroscopy (DS5 Edinburgh Instrument), respectively.

2.3. Bactericidal test

The bacterial strain used in this study is Gram-positive *S. aureus* ATCC 29213. The bacteria stored at -80 °C were thawed and activated by plating on TSA agar at 37 °C overnight. To ensure the purity of the strains, the *S. aureus* bacterial colony was selected, inoculated in TSB broth, and incubated at 37 °C for 24 hours. Subsequently, the bacterial suspension was diluted with phosphate-buffered saline (PBS) of 0.8 % NaCl, and its optical density was measured at a wavelength of 600 nm (OD_{600}). An OD_{600} value of 0.07 corresponded to a bacterial density of approximately 10^6 CFU/mL (colony-forming units per milliliter). The developed materials (γ-Fe_2O_3, α/γ-Fe_2O_3, and α-Fe_2O_3) were prepared at a concentration of 0.5 mg/mL, the test bacteria were added at an approximate density of 10^6 CFU/mL, and then the mixtures were exposed to blue light (460 nm, intensity of 80 W/m²) for 180 minutes. Bacterial

density and bactericidal efficacy were determined after 30 min intervals using the serial dilution spotting method [25]. The same experiments were repeated three times. The bacterial density at each time point was determined using Eq. (1), where A_i represents the average colony count, D_i denotes the dilution factor, and V indicates the volume of each droplet in milliliters (mL).

$$N_i\,(\text{CFU/mL}) = A_i(D_i/V) \quad (1)$$

The bactericidal effect at each time point was calculated using Eq. (2), where N_0 represents the initial bacterial, N_i denotes the bacterial density at time point t.

$$\text{Efficiency (\%)} = (N_0 - N_i)/N_0 \times 100\ \% \quad (2)$$

3. RESULTS AND DISCUSSION

3.1. Structural characteristics

The phase composition and crystal structures of the as-prepared samples γ-Fe_2O_3, α/γ-Fe_2O_3, and α-Fe_2O_3 were investigated by XRD pattern, as shown in Figure 2(a). The XRD pattern of γ-Fe_2O_3 demonstrated a cubic crystal structure (JCPDS# 39-1356) with five characterized peaks at 30.5, 35.7, 43.4, 57.6, and 63.3°, corresponding to the lattice planes (2 2 0), (3 1 1), (4 0 0), (5 1 1), and (4 4 0), respectively [26]. Meanwhile, the XRD peaks of α-Fe_2O_3 appear at 2θ values of 24.1, 33.2, 35.8, 40.8, 49.5, 54.2, 57.7, 62.6, and 64.1°, corresponding to the lattice planes of (012), (104), (110), (113), (024), (116), (018), (214), and (300) of the rhombohedral crystal structure (JCPDS# 33-0664) [15, 27]. Interestingly, the X-ray diffraction analysis of the α/γ-Fe_2O_3 sample distinctly reveals the co-occurrence of diffraction peaks, providing compelling evidence for the presence of both the γ-Fe_2O_3 and α-Fe_2O_3 phases. Notably, the peak at about 35.7° in the XRD pattern of α/γ-Fe_2O_3 is observed with a significantly broad base but a sharp tip. In the literature, this peak is known as an overlap of the (311) lattice plane of γ-Fe_2O_3 and the (110) lattice plane of α-Fe_2O_3 [23]. Therefore, to precisely ascertain the composition positions of the diffraction peaks corresponding to the (311) lattice plane of γ-Fe_2O_3 and the (110) lattice plane of α-Fe_2O_3, we performed peak deconvolution analysis on the XRD pattern of the α/γ-Fe_2O_3 sample at approximately 35.7°. The result of this analysis is depicted in Figure 2(b), and this revealed the difference from the peak positions of the (311) lattice plane of γ-Fe_2O_3 (at 35.69°) and the (110) lattice plane of α-Fe_2O_3 (at 35.79°) in the α/γ-Fe_2O_3 composite. Our deconvolution approach and findings here are in complete agreement with another study on the peak positions of α-Fe_2O_3 and γ-Fe_2O_3 within the α/γ-Fe_2O_3 bi-phase sample reported by Bi, Tao, Ren, Huang, WangHao [23]. Overall, these analyses confirm that there is a bi-phase mixture in our α/γ-Fe_2O_3 sample.

The calculation for determining the proportion of α-Fe_2O_3 and γ-Fe_2O_3 is performed using Eq. (3), where I_γ and I_α represent the diffraction intensities of the (311) plane of γ-Fe_2O_3 and the (104) plane of α-Fe_2O_3 in the α/γ-Fe_2O_3 sample, we were able to determine the phase percentages of γ-Fe_2O_3 and α-Fe_2O_3 to be 44 and 56 %, respectively [23, 24].

$$\%\ \alpha\text{-}Fe_2O_3 = 1/(1+1.7I_\gamma/I_\alpha) \quad (3)$$

In addition, to calculate the average crystallite size Scherrer's formula was used, as indicated by Eq. (4) [12], where D is the average crystallite size, λ is the wavelength (1.541 Å), θ is the Bragg diffraction angle, and β is the full-width half maximum (FWHM).

$$D = 0.9\lambda/[\beta\cos(\theta)] \quad (4)$$

Crystalline parameters were calculated from XRD data and Scherrer's formula by considering the prominent peak at (311) for γ-Fe_2O_3 and (110) for α-Fe_2O_3 in Table 1. The results showed that the γ-Fe_2O_3 sample had an initial crystallite size of about 9 nm. In the α/γ-Fe_2O_3 sample, the crystallite size of γ-Fe_2O_3 increased to 14.71 nm and α-Fe_2O_3 was about 30.26 nm. At 800 °C, the γ phase completely transformed into α-Fe_2O_3 and the α-Fe_2O_3 crystallite size increased to about 34.96 nm. It can be seen that the crystallite size increases as the calcination temperature increases.

Table 1. Crystalline parameters were calculated using XRD data and Scherrer's formula.

Sample	Phase	Crystal lattice	2θ position (°)	FWHM β (rad)	Crystallite size (nm)
γ-Fe2O3	γ	(3 1 1)	35.7	0.927	9.000
α/γ-Fe2O3	γ	(3 1 1)	35.69	0.569	14.709
	α	(1 0 4)	35.79	0.275	30.266
α-Fe2O3	α	(1 0 4)	35.8	0.238	34.962

The Raman analysis in Figure 2(c) reveals the characteristic peaks of γ-Fe_2O_3 at positions of 380, 490, and 680 cm^{-1} [28, 29]. At the same time, the α-Fe_2O_3 sample exhibits the characteristic peaks at 222, 291, and 406 cm^{-1} [30]. Particularly, the α/γ-Fe_2O_3 sample demonstrates discernible oscillatory behavior at 216, 280, and 390 cm^{-1}. This analysis reveals a pronounced blue shift in the oscillation of the α/γ-Fe_2O_3 sample compared to α-Fe_2O_3, which is similar to a recent publication by Tokubuchi *et al.* [31].

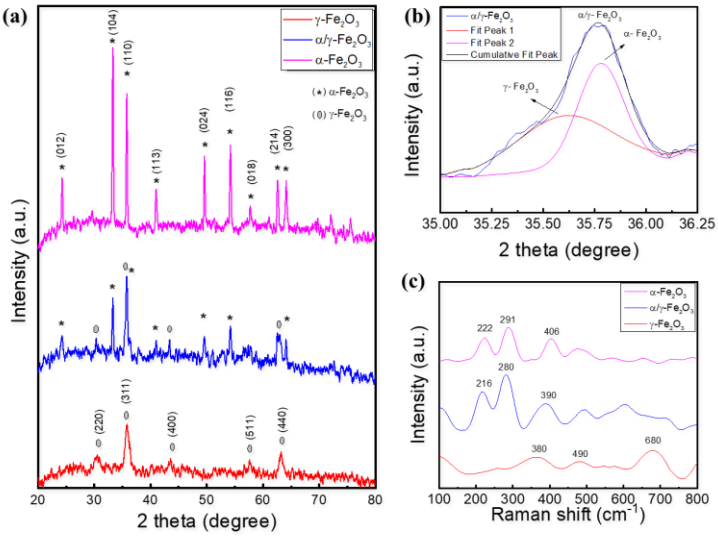

Figure 2. (a)XRD patterns of γ-Fe_2O_3, α/γ-Fe_2O_3, and α-Fe_2O_3; (b) Deconvolution of α/γ-Fe_2O_3 characteristic peak at ~35.75° to find its composition peaks, which are γ-Fe_2O_3 (Fit peak 1) and α-Fe_2O_3 (Fit peak 2); (c) Raman spectra of those samples.

3.2. Morphology analysis

The SEM image of the γ-Fe_2O_3 sample in Figure 3(a) shows the presence of γ-Fe_2O_3 nanoparticles ranging in size from 20-30 nm. In Figure 3(c), the α-Fe_2O_3 sample exhibited a coral-like morphology, similar to previous reports on α-Fe_2O_3 synthesis using the phase transition method [32]. The length and width of the α-Fe_2O_3 material are approximately 150-200

nm and 50-100 nm, respectively. The structural change in the crystal lattice of γ-Fe_2O_3 samples was seen at high temperatures [33]. Specifically, the cubic crystal structure of γ-Fe_2O_3 transforms into the rhombohedral one of α-Fe_2O_3, resulting in significant alterations in the morphological characteristics [34]. Reasonably, Figure 3(b) presents an SEM image of the calcined α/γ-Fe_2O_3 sample at 500 °C. At that temperature, the γ-Fe_2O_3 structure has incompletely converted to α-Fe_2O_3. Consequently, a coexistence of γ-Fe_2O_3 particles adhering to the network nodes of α-Fe_2O_3 is observed; here, Figures 3(d)-(f) reveal that there are contacts between the two types of Fe_2O_3 nanoparticles, which can be considered as bi-phase contacts [23, 35].

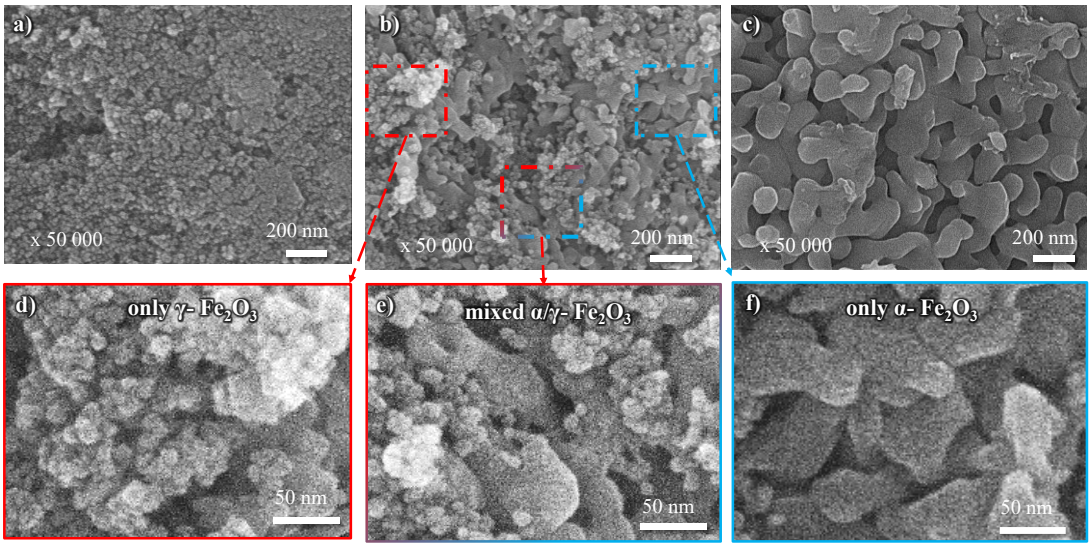

Figure 3. (a-c) SEM images of iron oxide materials produced at different temperatures: (a) γ-Fe_2O_3 after 200 °C; (b) α/γ-Fe_2O_3 after 500 °C; (c) α-Fe_2O_3 after 800 °C; (d)-(f) Magnified areas from the SEM image of α/γ-Fe_2O_3 after 500 °C, which show (left) a cluster of only γ-Fe_2O_3 nanoparticles, (middle) a cluster of α- and γ-Fe_2O_3 nanoparticles (i.e., bi-phase contact), and (right) a cluster of only α-Fe_2O_3.

3.3. Optical properties

The optical characteristics of the γ-Fe_2O_3, α/γ-Fe_2O_3, and α-Fe_2O_3 samples are represented by the UV-Vis spectra in Figure 4(a). The spectral analysis reveals absorption edges at around 575 nm and 740 nm for the γ-Fe_2O_3 and α-Fe_2O_3 samples, respectively. The absorption curve shapes of both γ-Fe_2O_3 and α-Fe_2O_3 found in this experiment closely resemble the shape reported in prior publications [36, 37]. Interestingly, the combination in the bi-phase α/γ-Fe_2O_3 material has led to changes in the shape of the absorption edge and peak compared to the pure γ-Fe_2O_3 or pure α-Fe_2O_3. In the literature, the optical absorption edge of an active material can be shifted due to the formation of a new phase or the phase transition of that material [23, 38-40]. According to our observation, the shifted absorption edge in our α/γ-Fe_2O_3 sample can be attributed to the following reasons, including the α phase formation in the γ-Fe_2O_3 nanoparticle matrix, as well as the phase transition of iron oxide from the γ phase to the α phase. In general, due to the structural changes (incompletely), the optical absorption spectrum of our bi-phase composite is slightly different from that of mono-phase Fe_2O_3 materials. Here, for further confirmation, we utilized the Tauc's method to estimate the optical band gap of our materials, as expressed in Eq. (5); where α, h, υ, B, and E_g are the absorption coefficient, Planck constant, light frequency, proportionality constant, and bandgap, respectively. Figure 4(b) presents the

$(\alpha h\upsilon)^2$ versus $h\upsilon$ plot, showing the bandgap energy of γ-Fe_2O_3, α/γ-Fe_2O_3, and α-Fe_2O_3 to be 2.32, 2.24, and 2.02 eV, respectively. This result implies that α/γ-Fe_2O_3 has a high photocatalytic potential in the visible light range [32].

$$(ah\upsilon)^2 = B(h\upsilon - E_g) \tag{5}$$

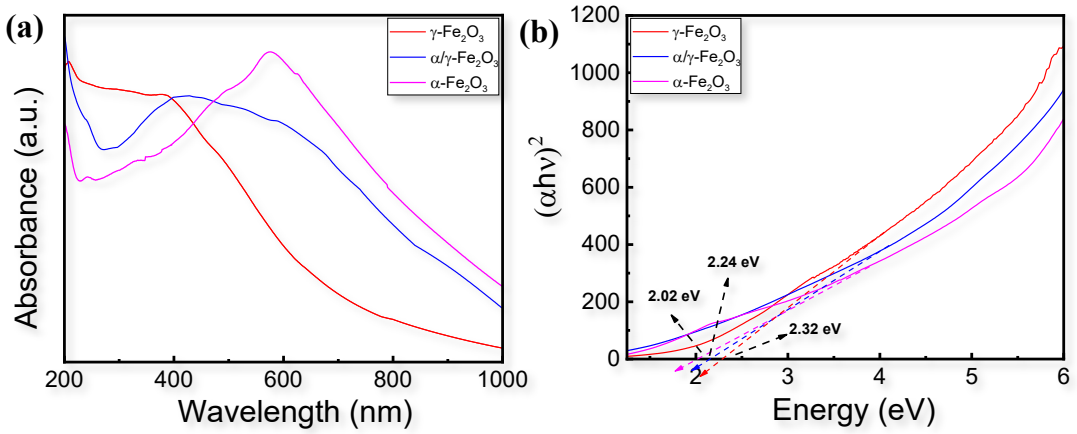

Figure 4. (a) UV–Vis absorption spectra and (b) Tauc plots [$(ah\upsilon)^2$vs$h\upsilon$] of γ-Fe_2O_3, α/γ-Fe_2O_3, and α-Fe_2O_3 materials.

3.4. Antibacterial activity

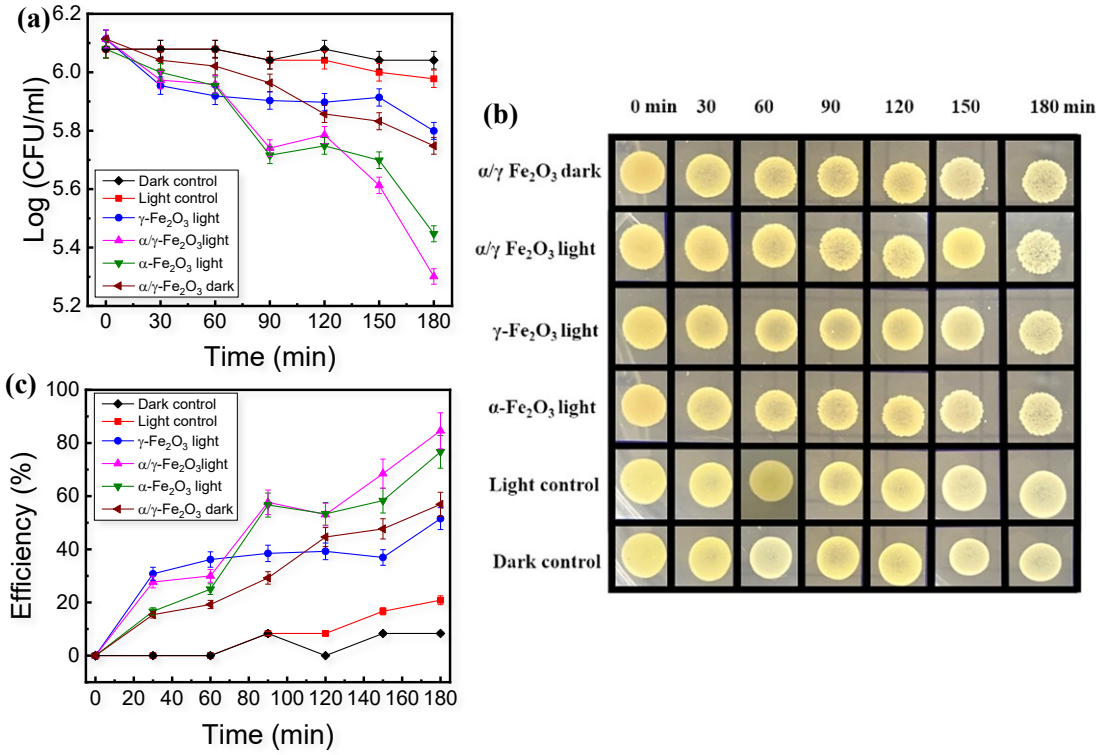

Figure 5. (a) Evaluation of the bacterial survivalability (Log (CFU/mL)) of three samples under light and dark conditions; (b) Photoimages showing their colonies in 10 µL over time; (c) Bactericidal efficiency over time against *S. aureus* bacterium when exposed to γ-Fe_2O_3, α/γ-Fe_2O_3, and α-Fe_2O_3.

Figure 5(a) shows the bacterial survival ability of the *S. aureus* (~10^6 CFU/mL) when exposed to γ-Fe_2O_3, α/γ-Fe_2O_3, or α-Fe_2O_3 at a concentration of 0.5 mg/mL for 180 minutes. After 30 min intervals, the samples were sequentially diluted with PBS (in 0.8 % NaCl solution) to achieve 10^{-1}, 10^{-2}, or 10^{-3} decimal concentrations, and so on, depending on the bacterial sample. Each dilution step by 10^{-1} was carried out by adding 1 mL of the sample (or solution from the previous dilution) into 9 mL of PBS in a test tube. The diluted samples were then dropped onto TSA agar plates and incubated at 37 °C for 24 hours. From the result of colony counting, the respective number is averaged. Figure 5(b) presents the counts of colonies in 10 µL over time. The α/γ-Fe_2O_3 material demonstrates a superior photocatalytic efficiency under illumination, resulting in the lowest bacterial density observed. Figure 5(c) shows the bactericidal effect of γ-Fe_2O_3, α/γ-Fe_2O_3, and α-Fe_2O_3 materials over time against *S. aureus*, which is confirmed by Eq. (2). These results indicate that α/γ-Fe_2O_3 exhibits a superior antibacterial ability compared to α-Fe_2O_3 and γ-Fe_2O_3. After 180 minutes of illumination, α/γ-Fe_2O_3 reduced the bacterial density of *S. aureus* from $6.11\log_{10}$ to $5.30\log_{10}$, achieving a bactericidal efficiency of 84.62 %. Meanwhile, the disinfectant abilities of γ-Fe_2O_3 and *α*-Fe_2O_3 were 51.54 and 76.67 %, respectively. The bactericidal efficiency of the bi-phase α/γ-Fe_2O_3 is 1.1 times higher than that of *α*-Fe_2O_3 and upto 1.6 times higher than that of the γ-Fe_2O_3.

3.5. Proposed bactericidal mechanism of α/γ-Fe_2O_3 composite

To explain the improved photocatalytic and bactericidal ability of our α/γ-Fe_2O_3 composite, we based on the electronic band structure to propose its mechanism. Particularly, the band edge positions of the conduction band (CB) and valence band (VB) of α-Fe_2O_3 and γ-Fe_2O_3 were estimated using empirical equations [41], noted as Eqs. (6) and (7).

$$E_{CB} = X - E_e - 0.5E_g \quad (6)$$

$$E_{VB} = E_{CB} + E_g \quad (7)$$

Here, E_e is the energy of free electrons on the hydrogen scale (E_e = 4.5 eV), and X is the absolute electronegativity of a semiconductor. The X values for α-Fe_2O_3 and γ-Fe_2O_3 are 4.78 and 5.87 eV, respectively [41, 42]. E_g is the band gap energy of the semiconductor, 2.02 eV for α-Fe_2O_3 and 2.32 eV for γ-Fe_2O_3. From these calculations, the E_{CB} values of α-Fe_2O_3 and γ-Fe_2O_3 were determined to be ca. -0.73 and 0.21 eV versus *NHE*, respectively, whereas the E_{VB} values were estimated to be 1.29 and 2.53 eV versus *NHE.* The bactericidal mechanism of the α/γ-Fe_2O_3 mixture is described in Figure 6. Under blue-light irradiation (λ = 460 nm), photo-induced free electrons and holes were generated inside the α/γ-Fe_2O_3 composite. At bi-phase contacts (between α- and γ- phases), electrons from the conduction band (CB) of α-Fe_2O_3 migrate to the CB of γ-Fe_2O_3 due to the potential difference. Meanwhile, holes move from the valence band (VB) of γ-Fe_2O_3 to the VB of α-Fe_2O_3. As a result, the electron-hole recombination mechanism in the bi-phase structure is significantly weakened [23, 24]. It is important to note that the CB energy level of γ-Fe_2O_3 (approximately 0.21 eV) is not sufficient to reduce O_2 into $^{\bullet}O_2^-$, as the reduction potential of $O_2/^{\bullet}O_2^-$ is -0.33 eV. Consequently, O_2 would directly react with photo-induced free electrons to produce H_2O_2, as illustrated in Eq. (8) [43]. On the other hand, the holes (h^+) in the VB of α-Fe_2O_3 may contribute to bacterial inactivation through direct oxidation of the cell membrane because their energy (approximately 1.29 eV) are

not sufficiently oxidizing to produce ˙OH radicals [43]. The oxidation potentials for $OH^-/{}^{\bullet}OH$ and $H_2O/{}^{\bullet}OH$ are 1.99 eV and 2.34 eV vs NHE, respectively [44].

$$2e^- + O_2 + 2H^+ \rightarrow H_2O_2 \quad (8)$$

In addition, Fenton reactions can occur due to the reductive dissolution of the material surface in aqueous environments, leading to the production of Fe^{2+} ions. These ions can then be oxidized in the presence of H_2O_2 to form Fe^{3+}, causing the decomposition of H_2O_2 into hydroxyl radicals [14], as illustrated in Eq. (9). Therefore, reactive oxygen species (ROS), predominantly comprising hydroxyl radicals (˙OH) and hydrogen peroxide (H_2O_2) interact with various components within bacterial cells, resulting in the destruction and demise of bacterial cells [18].

$$Fe^{2+} + H_2O_2 \rightarrow Fe^{3+} + {}^{\bullet}OH + HO^- \quad (9)$$

Besides, taking advantage of the thermally induced structural changes, particularly the formation of the bi-phase α/γ-Fe_2O_3 contact, our developed composite demonstrates more effective charge carrier separation and consequently ROS generation efficiency than single-phase materials.

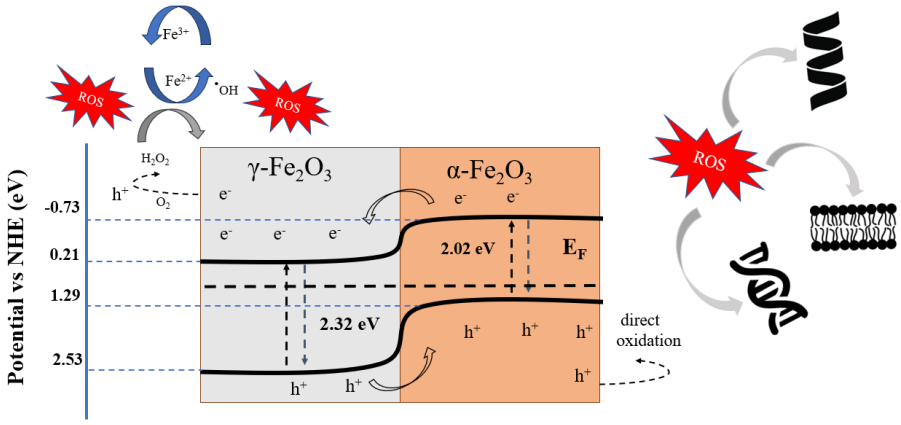

Figure 6. Bactericidal mechanism of α/γ-Fe_2O_3 mixture.

4. CONCLUSIONS

We have successfully developed a straightforward phase-transition technique for the synthesis of α/γ-Fe_2O_3 (a bi-phase composite). Due to the temperature-induced structural changes, especially the formation of bi-phase contacts between γ- and α- phases, this material shows the significantly reduced electron-hole recombination and improved photocatalytic efficiency. According to the findings, α/γ-Fe_2O_3 can kill bacteria with an excellent efficiency of up to 84.62 % within 180 minutes. As compared to the single-phase materials, the α/γ-Fe_2O_3 bi-phase mixture has a bactericidal efficiency about 1.1 times and 1.6 times higher than that of α-Fe_2O_3 and γ-Fe_2O_3, respectively. This critical finding implies that our bi-phase mixture has the potential to replace conventional single-phase materials in the field of photocatalysis.

Acknowledgments. This research was funded by Nguyen Tat Thanh University (NTTU) under grant number 2023.0126/HĐ-KHCN. Research facilities and equipment were supported by Nguyen Tat Thanh University, Ho Chi Minh City, Viet Nam.

CRediT authorship contribution statement. Tan Muon Dinh: Methodology, Investigation. Nguyen Thanh Loan: Resources, Investigation. Hoang Hung Nguyen: Formal analysis, Writing – original draft. Tran Viet Cuong: Formal analysis, Writing – original draft. Vinh Quang Dang: Formal analysis, Writing – original draft. Huynh Tran My Hoa: Conceptualization, Supervision, Writing – review & editing.

Declaration of competing interest. The authors declare that they have no known competing financial interests or personal relationships that could have appeared to influence the work reported in this paper.

REFERENCES

1. Lee A. S., de Lencastre H., Garau J., Kluytmans J., Malhotra-Kumar S., Peschel A., Harbarth S. - Methicillin-resistant *Staphylococcus aureus*. Nat. Rev. Dis. Primers, **4**(1) (2018) 1-23. https://doi.org/10.1038/nrdp.2018.33.
2. Zhou K., Li C., Chen D., Pan Y., Tao Y., Qu W., Liu Z., Wang X., Xie S. - A review on nanosystems as an effective approach against infections of *Staphylococcus aureus*. Int. J. Nanomed., **13** (2018) 7333-7347. https://doi.org/10.2147/ijn.s169935.
3. Guo Y., Song G., Sun M., Wang J., Wang Y. - Prevalence and therapies of antibiotic-resistance in *Staphylococcus aureus*. Front. Cell. Infect. Microbiol., **10** (2020) https://doi.org/10.3389/fcimb.2020.00107.
4. Cheung G. Y. C., Bae J. S., Otto M. - Pathogenicity and virulence of *Staphylococcus aureus*. Virulence, **12**(1) (2021) 547-569. https://doi.org/10.1080/21505594.2021.1878688.
5. Holck A. L., Liland K. H., Drømtorp S. M., Carlehög M., McLeod A. - Comparison of UV-c and pulsed UV light treatments for reduction of *salmonella*, *listeria monocytogenes*, and *enterohemorrhagic Escherichia coli* on eggs. J. Food Prot., **81**(1) (2018) 6-16. https://doi.org/10.4315/0362-028x.jfp-17-128.
6. Shoults D. C., Ashbolt N. J. - Decreased efficacy of UV inactivation of *Staphylococcus aureus* after multiple exposure and growth cycles. Int. J. Hyg. Environ. Health, **222**(1) (2019) 111-116. https://doi.org/10.1016/j.ijheh.2018.08.007.
7. Cunliffe A. J., Askew P. D., Stephan I., Iredale G., Cosemans P., Simmons L. M., Verran J., Redfern J. - How do we determine the efficacy of an antibacterial surface? A review of standardised antibacterial material testing methods. Antibiotics, **10**(9) (2021) 1069. https://doi.org/10.3390/antibiotics10091069.
8. Xu L., Zhang C., Xu P., Wang X. C. - Mechanisms of ultraviolet disinfection and chlorination of *Escherichia coli*: Culturability, membrane permeability, metabolism, and genetic damage. J. Environ. Sci., **65** (2018) 356-366. https://doi.org/10.1016/j.jes.2017.07.006.
9. Kim N.-H., Park W. B., Cho J. E., Choi Y. J., Choi S. J., Jun S. Y., Kang C. K., Song K.-H., Choe P. G., Bang J.-H., Kim E. S., Park S. W., Kim N.-J., Oh M.-d., Kim H. B. - Effects of phage endolysin SAL200 combined with antibiotics on *Staphylococcus aureus* infection. Antimicrob. Agents Chemother., **62**(10) (2018) e00731-00718. https://doi.org/10.1128/aac.00731-18.
10. Park K.-H., Han G. D., Neoh K. C., Kim T.-S., Shim J. H., Park H.-D. - Antibacterial activity of the thin ZnO film formed by atomic layer deposition under UV-A light. Chem. Eng. J., **328** (2017) 988-996. https://doi.org/10.1016/j.cej.2017.07.112.
11. Joost U., Juganson K., Visnapuu M., Mortimer M., Kahru A., Nõmmiste E., Joost U., Kisand V., Ivask A. - Photocatalytic antibacterial activity of nano-TiO_2 (anatase)-based thin films: Effects on *Escherichia coli* cells and fatty acids. J. Photochem. Photobiol. B: Biol., **142** (2015) 178-185. https://doi.org/10.1016/j.jphotobiol.2014.12.010.
12. Nguyen Van C. H., Nguyen H. K., Huynh H. Q., Pham H. A., Dinh T. M., Luong H. N., Phan B. T., Tran C. K., Dang V. Q. - Multi-modification of ZnO nanorods to enhance the visible absorption. Adv. Nat. Sci.: Nanosci. Nanotechnol., **11**(1) (2020) 015002. https://doi.org/10.1088/2043-6254/ab6290.

13. Tamirat A. G., Rick J., Dubale A. A., Su W.-N., Hwang B.-J. - Using hematite for photoelectrochemical water splitting: a review of current progress and challenges. Nanoscale Horiz., **1**(4) (2016) 243-267. https://doi.org/10.1039/c5nh00098j.
14. Araujo R. N., Nascimento E. P., Firmino H. C. T., Macedo D. A., Neves G. A., Morales M. A., Menezes R. R. - α-Fe_2O_3 fibers: An efficient photocatalyst for dye degradation under visible light. J. Alloys Compd., **882** (2021) 160683. https://doi.org/10.1016/j.jallcom.2021.160683.
15. Machala L., Tuček J., Zbořil R. - Polymorphous transformations of nanometric iron(III) oxide: a review. Chem. Mater., **23**(14) (2011) 3255-3272. https://doi.org/10.1021/cm200397g.
16. Rahmani M. B., Ghasemi E., Rezaii F. - Synthesis of wormlike α-Fe_2O_3 nanostructure: Characterization and antibacterial application. J. Electron. Mater., **49**(10) (2020) 6087-6095. https://doi.org/10.1007/s11664-020-08351-z.
17. Kurien U., Hu Z., Lee H., Dastoor A. P., Ariya P. A. - Radiation enhanced uptake of Hg0(g) on iron (oxyhydr)oxide nanoparticles. RSC Adv., **7**(71) (2017) 45010-45021. https://doi.org/10.1039/c7ra07401h.
18. Pallela P. N. V. K., Ummey S., Ruddaraju L. K., Gadi S., Cherukuri C. S., Barla S., Pammi S. V. N. - Antibacterial efficacy of green synthesized α-Fe_2O_3 nanoparticles using Sida cordifolia plant extract. Heliyon, **5**(11) (2019) e02765. https://doi.org/10.1016/j.heliyon.2019.e02765.
19. Rana P., Sharma S., Sharma R., Banerjee K. - Apple pectin supported superparamagnetic (γ-Fe_2O_3) maghemite nanoparticles with antimicrobial potency. Mater. Sci. Energy Technol., **2**(1) (2019) 15-21. https://doi.org/10.1016/j.mset.2018.09.001.
20. Bouziani A., Park J., Ozturk A. - Synthesis of α-Fe_2O_3/TiO_2 heterogeneous composites by the sol-gel process and their photocatalytic activity. J. Photochem. Photobiol. A: Chem., **400** (2020) 112718. https://doi.org/10.1016/j.jphotochem.2020.112718.
21. Li N., Zhang J., Tian Y., Zhao J., Zhang J., Zuo W. - Precisely controlled fabrication of magnetic 3D γ-Fe_2O_3@ZnO core-shell photocatalyst with enhanced activity: Ciprofloxacin degradation and mechanism insight. Chem. Eng. J., **308** (2017) 377-385. https://doi.org/10.1016/j.cej.2016.09.093.
22. Fu H., Sun S., Yang X., Li W., An X., Zhang H., Dong Y., Jiang X., Yu A. - A facile coating method to construct uniform porous α-Fe_2O_3@TiO_2 core-shell nanostructures with enhanced solar light photocatalytic activity. Powder Technol., **328** (2018) 389-396. https://doi.org/10.1016/j.powtec.2018.01.067.
23. Bi J., Tao Q., Ren J., Huang X., Wang T., Hao H. - P25-inspired α/γ-Fe_2O_3 isoelement heterostructures for visible-light photocatalysis: Optimization of crystalline ratios and mechanism investigation. J. Alloys Compd., **937** (2023) 168422. https://doi.org/10.1016/j.jallcom.2022.168422.
24. Wei Z., Wei X., Wang S., He D. - Preparation and visible-light photocatalytic activity of α-Fe_2O_3/γ-Fe_2O_3 magnetic heterophase photocatalyst. Mater. Lett., **118** (2014) 107-110. https://doi.org/10.1016/j.matlet.2013.12.051.
25. Paluszynski J. P., Klassen R., Meinhardt F. - Genetic prerequisites for additive or synergistic actions of 5-fluorocytosine and fluconazole in baker's yeast. Microbiology, **154**(10) (2008) 3154-3164. https://doi.org/10.1099/mic.0.2008/020107-0.
26. Aslam M., Qamar M. T., Rehman A. U., Soomro M. T., Ali S., Ismail I. M. I., Hameed A. - The evaluation of the photocatalytic activity of magnetic and non-magnetic polymorphs of Fe_2O_3 in natural sunlight exposure: A comparison of photocatalytic activity. Appl. Surf. Sci., **451** (2018) 128-140. https://doi.org/10.1016/j.apsusc.2018.04.219.
27. Kushwaha P., Chauhan P. - Synthesis of spherical and Rod-Like EDTA assisted α-Fe_2O_3 nanoparticles via Co-precipitation method. Mater. Today: Proc., **44** (2021) 3086-3090. https://doi.org/10.1016/j.matpr.2021.02.450.

28. Wu H., Wu G., Wang L. - Peculiar porous α-Fe_2O_3, γ-Fe_2O_3 and Fe_3O_4 nanospheres: Facile synthesis and electromagnetic properties. Powder Technol., **269** (2015) 443-451. https://doi.org/10.1016/j.powtec.2014.09.045.
29. Marycz K., Sobierajska P., Wiglusz R., Idczak R., Nedelec J.-M., Fal A., Kornicka-Garbowska K. - Fe_3O_4 magnetic nanoparticles under static magnetic field improve osteogenesis via RUNX-2 and inhibit osteoclastogenesis by the induction of apoptosis. Int. J. Nanomed., **15** (2020) 10127-10148. https://doi.org/10.2147/ijn.s256542.
30. Zhang X., Niu Y., Meng X., Li Y., Zhao J. - Structural evolution and characteristics of the phase transformations between α-Fe_2O_3, Fe_3O_4 and γ-Fe_2O_3 nanoparticles under reducing and oxidizing atmospheres. CrystEngComm, **15**(40) (2013) 8166-8172. https://doi.org/10.1039/c3ce41269e.
31. Tokubuchi T., Arbi R. I., Zhenhua P., Katayama K., Turak A., Sohn W. Y. - Enhanced photoelectrochemical water splitting efficiency of hematite (α-Fe_2O_3)-Based photoelectrode by the introduction of maghemite (γ-Fe_2O_3) nanoparticles. J. Photochem. Photobiol. A: Chem., **410** (2021) 113179. https://doi.org/10.1016/j.jphotochem.2021.113179.
32. Gupta N. K., Ghaffari Y., Bae J., Kim K. S. - Synthesis of coral-like α-Fe_2O_3 nanoparticles for dye degradation at neutral pH. J. Mol. Liq., **301** (2020) 112473. https://doi.org/10.1016/j.molliq.2020.112473.
33. Farbod M., Movahed A., Kazeminezhad I. - An investigation of structural phase transformation of monosize γ-Fe_2O_3 nanoparticles fabricated by arc discharge method. Mater. Lett., **89** (2012) 140-142. https://doi.org/10.1016/j.matlet.2012.08.091.
34. Cao Y., Zheng X., Du Z., Shen L., Zheng Y., Au C., Jiang L. - Low-temperature H_2S removal from gas streams over γ-FeOOH, γ-Fe_2O_3, and α-Fe_2O_3: Effects of the hydroxyl group, defect, and specific surface area. Ind. Eng. Chem. Res., **58**(42) (2019) 19353-19360. https://doi.org/10.1021/acs.iecr.9b03430.
35. Ghasemifard M., Heidari G., Ghamari M., Fathi E., Izi M. - Synthesis of porous network-like α-Fe_2O_3 and α/γ-Fe_2O_3 nanoparticles and investigation of their photocatalytic properties. Nanotechnologies Russ., **14**(7–8) (2019) 353-361. https://doi.org/10.1134/s1995078019040062.
36. Shi Y., Li H., Wang L., Shen W., Chen H. - Novel α-Fe_2O_3/CdS cornlike nanorods with enhanced photocatalytic performance. ACS Appl. Mater. Interfaces, **4**(9) (2012) 4800-4806. https://doi.org/10.1021/am3011516.
37. Chen K. L., Yeh Y. W., Liao S., Wu C. H., Wang L. M. - 2016 IEEE 16th international conference on nanotechnology (IEEE-NANO), (2016)
38. Liang Y.-C., Hsu Y.-W. - Enhanced sensing ability of brush-like Fe_2O_3-ZnO nanostructures towards NO_2 gas via manipulating material synergistic effect. Int. J. Mol. Sci., **22**(13) (2021) 6884. https://doi.org/10.3390/ijms22136884.
39. Mei Q., Zhang F., Wang N., Yang Y., Wu R., Wang W. - TiO_2/Fe_2O_3 heterostructures with enhanced photocatalytic reduction of Cr(VI) under visible light irradiation. RSC Adv., **9**(39) (2019) 22764-22771. https://doi.org/10.1039/c9ra03531a.
40. Yang Y., Zhang T., Le L., Ruan X., Fang P., Pan C., Xiong R., Shi J., Wei J. - Quick and facile preparation of visible light-Driven TiO_2 photocatalyst with high absorption and photocatalytic activity. Sci. Rep., **4**(1) (2014) 7045. https://doi.org/10.1038/srep07045.
41. Li C., Yu S., Che H., Zhang X., Han J., Mao Y., Wang Y., Liu C., Dong H. - Fabrication of z-scheme heterojunction by anchoring mesoporous γ-Fe_2O_3 nanospheres on g-C_3N_4 for degrading tetracycline hydrochloride in water. ACS Sustain. Chem. Eng., **6**(12) (2018) 16437-16447. https://doi.org/10.1021/acssuschemeng.8b03500.
42. Zheng J., Liu G., Jiao Z. - Highly efficient photo-fenton ag/Fe_2O_3/BiOI z-scheme heterojunction for the promoted degradation of tetracycline. Nanomaterials, **13**(13) (2023) 1991. https://doi.org/10.3390/nano13131991.

43. Ng T. W., Zhang L., Liu J., Huang G., Wang W., Wong P. K. - Visible-light-driven photocatalytic inactivation of *Escherichia coli* by magnetic Fe_2O_3–AgBr. Water Res., **90** (2016) 111-118. https://doi.org/10.1016/j.watres.2015.12.022.
44. Yang H., He D., Liu C., Zhang T., Qu J., Jin D., Zhang K., Lv Y., Zhang Z., Zhang Y.-n. - Visible-light-driven photocatalytic disinfection by S-scheme α-Fe_2O_3/g-C_3N_4 heterojunction: Bactericidal performance and mechanism insight. Chemosphere, **287** (2022) 132072. https://doi.org/10.1016/j.chemosphere.2021.132072.